

EXPERIMENTAL AND NUMERICAL INVESTIGATIONS OF SIZE EFFECTS IN REINFORCED CONCRETE BEAMS WITH STEEL OR BASALT BARS

E. KOROL AND J. TEJCHMAN

Gdansk University of Technology, Civil and Environmental Engineering Department
Narutowicza 11/12, 80-233 Gdańsk-Wrzeszcz
e-mail: ewelina.korol@pg.gda.pl, tejchmk@pg.gda.pl

Key words: basalt bars, FE simulation, fracture, random fields, RC beams, size effect, steel bars.

Abstract: Experimental and numerical investigations on size effects in reinforced concrete beams of a similar geometry were performed. Laboratory tests were carried out on over-reinforced concrete beams with steel or basalt bars and without shear reinforcement. The beams were geometrically similar. In laboratory tests, load-deflection curves and cracks were registered. In addition, a Digital Image Correlation technique was used to measure displacements on the outer concrete surface. FE numerical analyses of a size effect on the shear strength were carried out with an isotropic elasto-plastic model with non-local softening. The bond-slip behaviour between bars and concrete was simulated. Deterministic and statistical FE simulations taking into account a spatial variability of the local tensile strength were performed in order to determine in numbers the deterministic and statistical size effect.

1 INTRODUCTION

A size effect in concrete causes that both the nominal structural strength σ_N and material brittleness (ratio between the energy consumed during the loading process after and before the stress-strain peak) decrease with increasing characteristic specimen dimension D ([1], [2], [3]). Thus, concrete becomes ductile on a small scale and perfectly brittle on a sufficiently large scale. According to Bazant ([1], [3]) the reasons of this behaviour are: a) the presence of intense strain localization regions with a certain volume (i.e. micro-crack regions), called also the fracture process zone FPZ), which precede macro-cracks and contribute to a deterministic size effect and b) a random distribution of material properties contributing to a statistical size effect. In turn, Carpinteri [2] postulated that the reason of a size effect in concrete structures was the multi-fractality of a fracture surface which increased with a spreading material disorder in large structures.

A strong size effect occurs among others in reinforced concrete beams without shear reinforcement wherein a diagonal shear-tensile fracture mechanism occurs. Such behaviour was experimentally observed among others by Leonhardt and Walther [4], Kani ([5], [6]), Bhal [7], Taylor [8], Walraven [9], Chana [10], Iguro et al. [11], Bazant and Kazemi, [12], Shioya et.al. [13], Kim and Park [14], Grimm [15], Ghannoum [16], Kawano and Watanabe [17], Podgorniak-Stanik [18], Yoshida [19], Lubell et al. [20] and Korol [21]. The diagonal cracks at failure have in experimental tests essentially similar paths and relative lengths at the maximum load independently of the beam size. Therefore, the size effect in these beams can be described by the deterministic (energetic) size effect law (SEL) of Type II following Bazant [1], being valid for structures of a positive similar geometry possessing large stress-free cracks that grow in a stable manner up to the maximum load

$$v_c(D) = \frac{v_0}{\sqrt{1 + \frac{D}{D_0}}} \quad (1)$$

where is v_c the shear strength ($v_c = V/tD$, V - the ultimate shear force, t - the specimen thickness) and v_0 and D_0 are the empirical parameters to be determined by fitting Eq.1 to experimental results.

2 EXPERIMENTAL TESTS

The laboratory experiments were conducted on geometrically similar over-reinforced rectangular concrete free-supported beams with three different sizes. The slender specimens (SL) with longitudinal steel reinforcement were subjected to four-point bending with the shear span to the effective depth ratio $a/D=3$ (Fig.1). In turn, the short beams (SH) were reinforced with composite basalt bars (BFRP) and tested under three-point bending at $a/D=1$ (Fig.2). The beams were scaled in two dimensions: length and height, while the thickness was kept always constant $t=200$ mm.

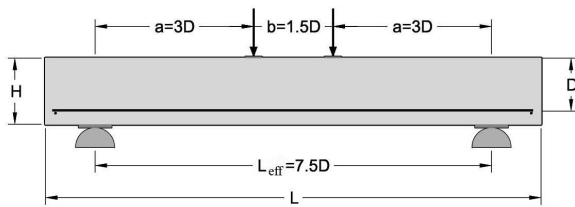


Figure 1: Geometry and loading of slender concrete beams with steel bars

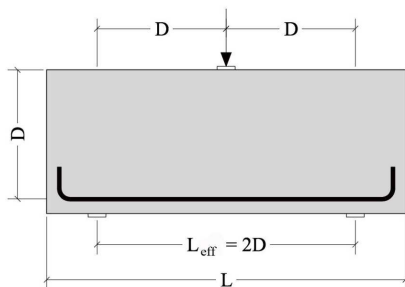


Figure 2: Geometry and loading of short concrete beams with BFRP bars

2.1 Experimental set up

The slender beams were made from the concrete C35/45 with the maximum aggregate size $d_{max}=16$ mm. The reinforcement ratio was $\rho=1\%$ and the steel yielding strength $f_{yd}=500$ MPa. The specimens were classified according to their height and were denoted as SL20, SL40 and SL80 (Fig.3). The small beams SL20 had the height $H=200$ mm and length $L=1500$ mm, the medium beams SL40: $H=400$ mm and $L=3000$ mm and the large beams SL80: $H=800$ mm and $L=6000$ mm. For each beam size 3 specimens were tested.

The short BFRP beams were casted from the concrete C16/20 with the maximum aggregate size $d_{max}=16$ mm (Fig.4). The reinforcement ratio was $\rho=0.63\%$ with the tensile strength of 1100 MPa and the elastic modulus of 70 GPa. The beams were divided into three groups: SH22 with $H=22$ mm and $L=640$ mm, SH40 with $H=400$ mm and $L=1000$ mm and SH78 with $H=780$ mm and $L=1800$ mm.

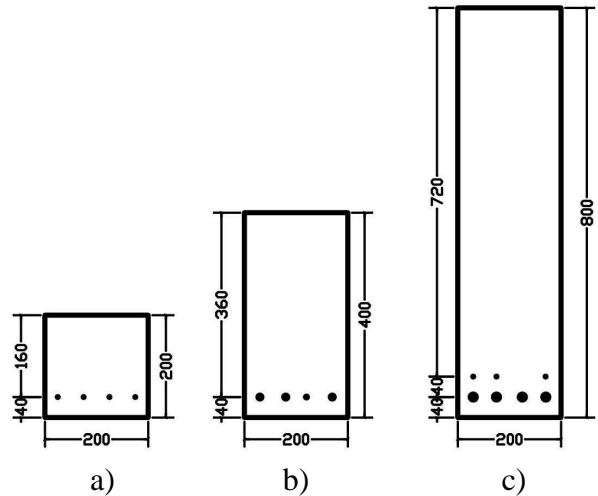


Figure 3: Cross-section of slender RC beams: a) SL20, b) SL40 and c) SL80

During tests several LVDT gauges were used to measure the true deflection at the mid-span, strain in the compression zone and crack extension. Simultaneously, the non-invasive Digital Image Correlation (DIC) technique [21] was applied to register a propagation of localized zones on the concrete surface (e.g. 7 digital cameras were used to capture strain

localization in the largest RC beams SL80). The images had the resolution $3888 \text{ pixels} \times 2592 \text{ pixels}$. The area of $1 \times 1 \text{ mm}^2$ on a concrete surface was represented in the image by $15 \text{ pixels} \times 15 \text{ pixels}$.

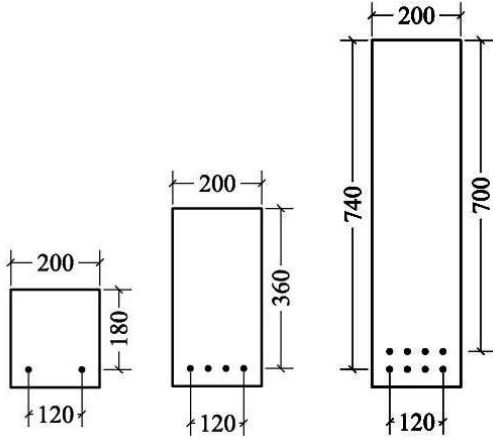


Figure 4: Cross-section of short concrete beams with BFRP bars: a) SH22, b) SH40 and c) SL78

2.2 Test results

The slender RC beams failed due to the diagonal-tension failure preceded first by a propagation of an inclined crack at the mid-shear span and next by a development of a horizontal splitting crack along the horizontal reinforcement. A strong size effect on the nominal shear strength of RC beams was obtained. The mean nominal shear strength decreased from $v_c=1.44 \text{ MPa}$ in SL20 ($D=160 \text{ mm}$) and $v_c=1.19 \text{ MP}$ in SL40 ($D=360 \text{ mm}$) down to $v_c=0.88 \text{ MPa}$ in the SL80 ($D=750 \text{ mm}$). Thus, the strength reduction was 40%. The results were compared to the analytical formula of size effect SEL Type II by Bazant (Fig.5) (with $v_0=1.91$ and $D_0=212.76$ in Eq.1). The mean square error was solely $6.27e-3$.

In all slender RC beams, a similar crack pattern was observed (Fig.6). The critical inclined crack always occurred at the mid-shear span a . The distance between the critical inclined crack and support c (measured at the beam mid-height) related to the shear span a (c/a) was: 0.54-0.61 (SL20), 0.54-0.61 (SL40) and 0.52-0.58 (SL80), respectively. The height of the cracks was $0.864 \times H$, $0.816 \times H$ and $0.836 \times H$ for SL20, SL40 and SL80,

respectively. A similar crack distribution occurred on both concrete beam sides (Fig.7).

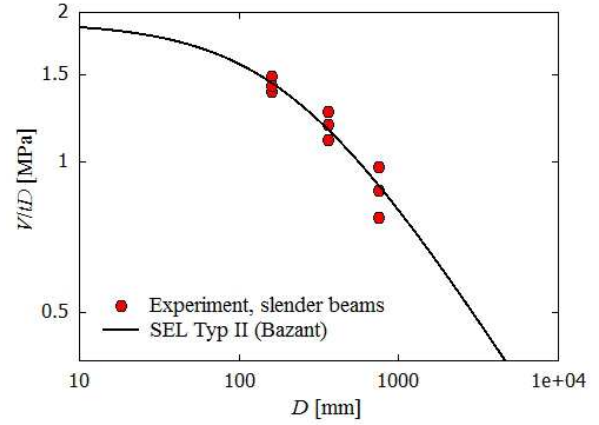


Figure 5: Nominal shear strength of slender RC beams from experiments compared to SEL by Bazant

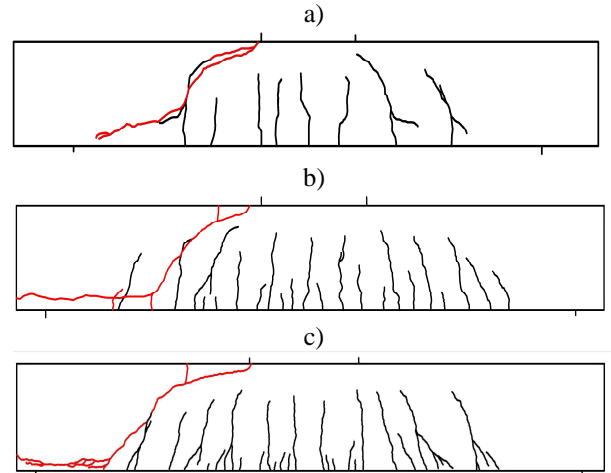


Figure 6: Experimental crack pattern in slender RC beams: SL20 (a), SL40 (b) and SL80 (c) (note that beams are not properly scaled)

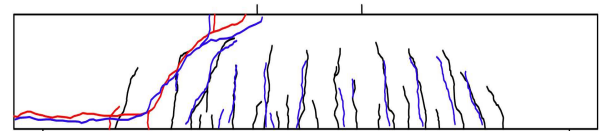


Figure 7: Crack pattern on front side (black and red colour) and back side (blue colour) in RC beam SL40

The localized zone pattern registered with the DIC technique on the concrete surface of a slender RC beam SL20 during failure is shown in Fig.8. The width of localized zones varied between $(1-1.5) \times d_{\max}$ and was independent of the beam size.

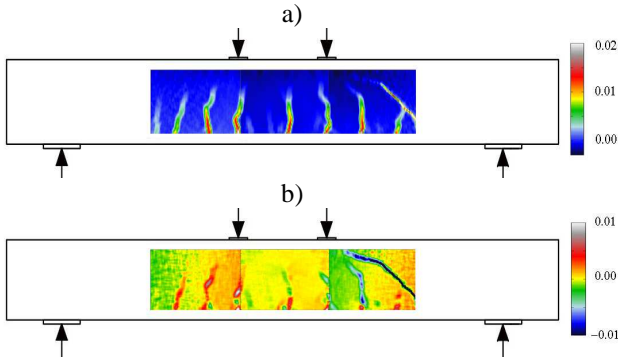


Figure 8: Localized zones measured with DIC on the concrete surface of slender RC beam SL20: distribution of normal strain ε_{xx} (a) and shear strain ε_{xy} (b)

The short BFRP beams failed in shear in a sudden and abrupt manner. The effect of the beam size on the nominal shear strength was greater than in slender RC beams (Fig.9). The shear strength decreased from $v_c=4.73$ MPa (SH22, $D=180$ mm) and 2.99 MPa (SH40, $D=360$ mm) down to 1.78 MPa (SH78, $D=780$ mm). Hence, the reduction exceeded 60%, whereas the beam effective depth D increased 4 times.

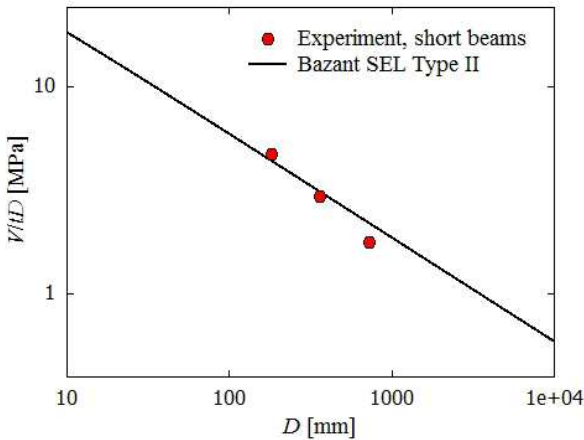


Figure 9: Nominal shear strength of short BFRP beams from experiment compared to SEL by Bazant

The short BFRP beams had significantly higher crack widths (reaching 4 mm before failure in SH22, Fig.10) than slender RC beams (about 0.2 mm before failure). Besides, the mid-span deflection in short beams (6.5-7.5 mm) was also larger than in slender beams in spite of the higher ratio H/L_{eff} in short beams. By comparing experimental results with SEL Type II by Bazant (Eq.1 with

$v_0=76.26$ and $D_0=0.607$), it can be observed that the predicted size effect relationship in a double logarithmic scale is represented by a straight line. Hence, the size effect in short BFRP beams indicating very high material brittleness beams can captured by the Linear Elastic Fracture Mechanics LEFM,

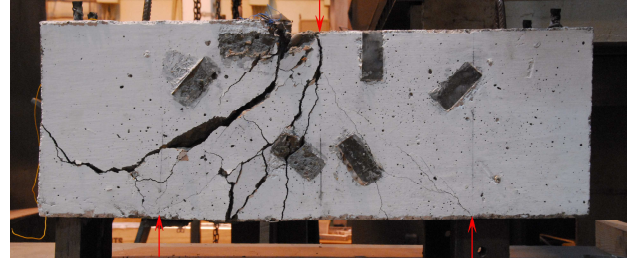


Figure 10: Short BFRP beam SH22 after failure

3 NUMERICAL INVESTIGATIONS

The numerical FE analyses were performed with slender concrete beams longitudinally reinforced with steel bars (Section 2) under plain stress conditions. Both deterministic and statistical (stochastic) simulations were carried out. In deterministic studies, the local material tensile strength f_t was assumed to be constant and uniformly distributed in the entire specimen. In statistical simulations, a spatial fluctuation of the local material tensile strength was taken into account [22]). The spatially correlated random fields described by a Gauss distribution function and squared exponential correlation function were used.

3.1 Constitutive model

Concrete was described with an isotropic elasto-plastic constitutive model with non-local softening ([23], [24]). To describe its behaviour under tension, the Rankine yield function f with isotropic softening was assumed:

$$f = \max\{\sigma_1, \sigma_2, \sigma_3\} - \sigma_t(\kappa_1), \quad (2)$$

where: σ_i are the principal stresses ($i=1-3$), σ_t is the tensile yield stress and κ_1 denotes the softening parameter equal to the maximum principal plastic strain. The associated flow rule was assumed. To model the concrete

softening under tension, the exponential curve by Hordijk [25] was chosen. In a compression regime, the shear yield surface based on the linear Drucker-Prager criterion with isotropic hardening/softening was assumed

$$f_1 = q + p \tan \varphi - \left(1 - \frac{1}{3} \tan \varphi\right) \sigma_c(\kappa_2) \quad (3)$$

$$q = \sqrt{\frac{3}{2}} s_{ij} s_{ij} \text{ and } p = \frac{1}{3} \sigma_{kk}, \quad (4)$$

where: q – the Mises equivalent deviatoric stress, p – the mean stress and φ – the internal friction angle and s_{ij} – the deviator of the stress tensor σ_{ij} . The material hardening/softening was defined by the evolution of the uniaxial compression stress $\sigma_c(\kappa_2)$. The internal friction angle φ was assumed as

$$\tan \varphi = \frac{3(1 - r_{bc}^\sigma)}{1 - 2r_{bc}^\sigma}, \quad (5)$$

with r_{bc}^σ as the ratio between the uniaxial compressive strength and biaxial compressive strength ($r_{bc}^\sigma = 1.2$). The flow potential was defined as

$$g_1 = q + p \tan \psi, \quad (6)$$

wherein ψ is the dilatancy angle ($\psi \neq \varphi$).

A non-local theory was used as a regularization technique with the non-local softening parameters $\bar{\kappa}_i(\mathbf{x})$ ($i=1, 2$) defined after Brinkgreve [26]

$$\bar{\kappa}_i(\mathbf{x}) = (1 - m)\kappa_i(\mathbf{x}) + m \frac{\int_V \omega(\|\mathbf{x} - \boldsymbol{\xi}\|) \kappa_i(\boldsymbol{\xi}) d\boldsymbol{\xi}}{\int_V \omega(\|\mathbf{x} - \boldsymbol{\xi}\|) d\boldsymbol{\xi}} \quad (7)$$

where V denotes the body volume, \mathbf{x} are the coordinates of the considered point, $\boldsymbol{\xi}$ are the coordinates of the surrounding points, ω denotes the weighting function taken as Gauss distribution function (Eq.8)

$$\omega(r) = \frac{1}{l_c \sqrt{\pi}} e^{-\left(\frac{r}{l_c}\right)^2}, \quad (8)$$

where l_c is the characteristic length of micro-structure and r is the distance between material points.

The behaviour of steel bars was elasto-perfect plastic described with the von Mises criterion

$$f_s(\boldsymbol{\sigma}, \kappa_s) = q - \sigma_s(\kappa_s), \quad (9)$$

where σ_s is the yield stress for steel and κ_s is the hardening parameter.

To simulate an interaction between concrete and reinforcement, a bond-slip relationship was defined. An interface with a zero thickness was assumed along a contact surface. In order to describe the splitting bond failure along reinforcement, the model by Akkerman [27] was used being a modification of the original model proposed by den Uijl and Bigaj [28]. The model takes into account the evolution of the radial stress $\sigma_{r,rs}$ versus the radial strain $\varepsilon_{r,rs}$ and is divided into 3 phases (Eq.10). The first phase (I) ($0 \leq \varepsilon_{r,rs} \leq \varepsilon_{r,rs,max}$) characterizes a non-linear material behaviour caused by cracks, the second one (II) ($\varepsilon_{r,rs,max} < \varepsilon_{r,rs} \leq \varepsilon_{r,rs,res}$) includes linear softening and the third one (III) ($\varepsilon_{r,rs,res} < \varepsilon_{r,rs}$) considers the residual strength

$$\sigma_{r,rs}(\varepsilon_{r,rs}) = \begin{cases} \sigma_{r,rs,max} \frac{k\eta - \eta^2}{1 + (k-2)\eta} & \text{(I)} \\ \sigma_{r,rs,max} \left(1 - \frac{1-\psi}{\varepsilon_{r,rs} - \varepsilon_{r,rs,max}} (\varepsilon_{r,rs} - \varepsilon_{r,rs,max})\right) & \text{(II)} \\ \sigma_{r,rs,res} & \text{(III)} \end{cases} \quad (10)$$

with the parameters

$$k = \frac{E_r \varepsilon_{r,rs,max}}{\sigma_{r,rs,max}} \text{ and } \eta = \frac{\varepsilon_{r,rs}}{\varepsilon_{r,rs,max}}. \quad (11)$$

The phase limits were defined by radial strain and stress values

$$\varepsilon_{r,rs,\max} = 4.2 \frac{f_t}{E} \left(\frac{c_{eff}}{\phi_b} \right)^{1.08},$$

$$\sigma_{r,rs,\max} = 2f_t \left(\frac{c_{eff}}{\phi_b} \right)^{0.88}. \quad (12)$$

$$\varepsilon_{r,rs,\max} = \frac{f_t}{E} \left(\frac{2c_{eff}}{\phi_b} + \frac{c_0}{\phi_b} \right),$$

$$\sigma_{r,rs,rs} = \psi_b \sigma_{r,rs,\max} \quad \text{with } \psi_b=0.2 \quad (13)$$

where c_{eff} is the effective concrete cover, ϕ_b is the bar diameter and c_0 is the empirical parameter affecting softening in the second phase (Eq.10). The radial strain $\varepsilon_{r,rs}$ was the function of the slip displacement δ

$$\varepsilon_{r,rs}(\delta) = \frac{2\delta}{\phi_b} \tan \vartheta_b \quad \text{with } \nu_b = 0.1f_c. \quad (14)$$

3.2 FE input data

The FE mesh included plane stress quadrilateral elements composed of four diagonally crossed triangles. The FE elements had the area 1.5×2.0 mm (width \times height) along the beam span L_{eff} for SL20 and SL40. In the case of the beams SL80 the mesh was finer at the mid-span covering $0.8 \times L_{eff}$. In total, 13'600-169'344 finite elements were used depending upon the beam size. The steel bars were modelled with 2D elements of the width 1.5 mm and height 2-2.5 mm depending on the bar diameter ϕ_b . The following constants were adopted for the isotropic elasto-plastic model for concrete (Eqs.2-6): uniaxial tensile strength $f_t=2.2$ MPa, uniaxial compression strength $f_c=35$ MPa, Young modulus $E=34$ GPa and Poisson's ratio $\nu=0.2$. The internal friction angle was $\varphi=14^\circ$ and the dilatancy angle $\psi=8^\circ$. The tensile fracture energy was $G_f=130$ N/m and the compressive fracture energy $G_c=1300$ N/m. The calculations were carried out with the characteristic length of $l_c=5$ mm based on the experimentally measured mean width of localized zones by

means of the DIC technique equal to 20 mm. The non-locality parameter was $m=2$ [29]. In the bond-slip relationship by Akkermann [27], the parameters were $c_{eff}=22$ mm and $c_0=0.18$ (Eqs.10-13).

In statistical simulations, random fields were used to model a local fluctuation of the uniaxial tensile strength. A truncated Gauss probability distribution function was assumed. The mean tensile strength was the same as in deterministic simulation $f_t=2.2$ MPa, while the standard deviation was $\sigma_{f_t}=0.264$ MPa giving the coefficient of variation $cov_{f_t}=0.12$ calculated as σ_{f_t}/f_t . The spatial correlation describing a dependence of any two points at the distance $|x_1-x_2|$ was defined by the homogenous square exponential autocorrelation function

$$C(x_1, x_2) = \exp\left(-\frac{(x_1 - x_2)^2}{l^2}\right) \quad (15)$$

with the length of correlation $l=100$ mm corresponding to 5 times the mean width of localized zones obtained from DIC measurements.

The random fields were generated using the Karhunen-Loève expansion ([30], [31]) and the wavelet-Galerkin approach proposed by Phoon et al. ([32], [33]). The wavelets were used to construct the orthogonal basis for eigenfunctions. Initially 2000 random fields were generated to reproduce the desired autocorrelation function. Next, using the stratified sampling (SS) technique 12 samples were chosen for further FE analyses. The SS method was based on a sampling parameter defined as the mean value of a random field in the shear span area. The random field discretization was the same as the FE mesh.

3.3 Numerical results

Deterministic simulations

The deterministic results showed a significant effect of the beam effective depth on the nominal shear strength (Fig.11). The calculated nominal shear strengths of all beam sizes were consistent with the mean

experimental values and were: $v_c=1.43$ MPa, $v_c=1.170$ MPa and $v_c=0.88$ MPa in the beam SL20, SL40 and SL80, respectively. The deterministic results fitted well the experimentally calibrated SEL by Bazant.

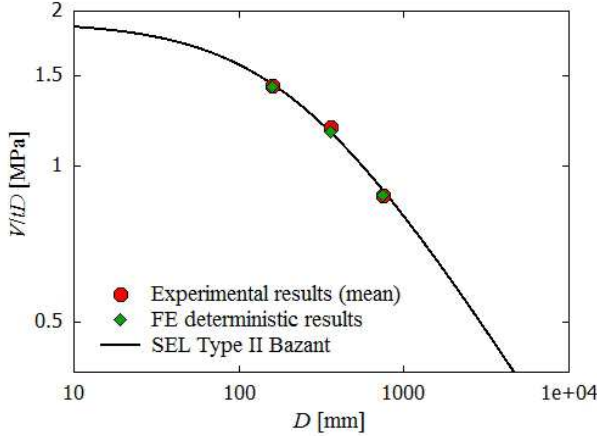


Figure 11: Nominal shear strengths of slender RC beams from experimental and FE deterministic investigations compared to SEL of Type II by Bazant

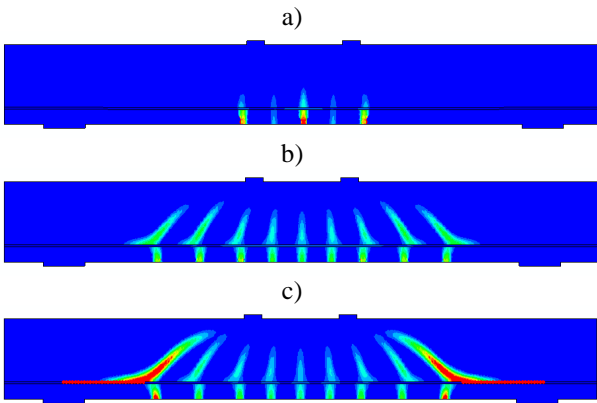


Figure 12: Localized zones in beam SL20 from deterministic FE simulation at: 30% (a), 55% (b), 90% (c) and 100% (d) of peak load

The strain localization process in all beams took place in a similar way (Fig.12). First, straight localized zones appeared in the region of a constant bending moment. Next, some inclined zones developed in the shear area. Finally, starting together with a diagonal localized zone, the bond failure of a splitting type took place and developed along a contact surface towards the support. The failure mechanism was similar as the experimental one.

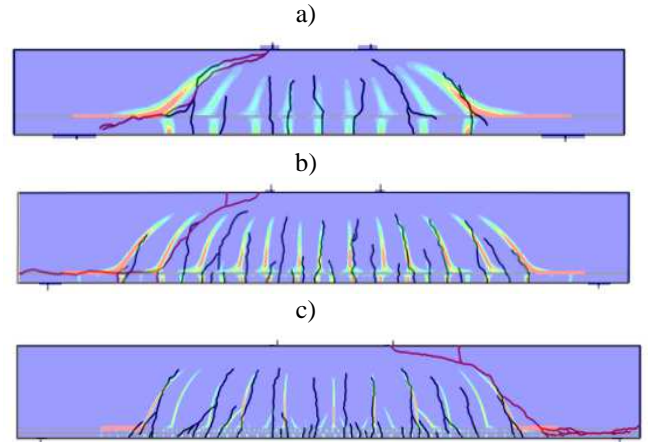


Figure 13: Calculated localized zones in deterministic simulations compared to experimental crack pattern in beams: SL20 (a), SL40 (b) and SL80 (c) (note that beams are not properly scaled)

The localized zones obtained in deterministic simulations and experimental cracks paths in the beams: SL20, SL40 and SL80 were compared together in Figure 13. The height, spacing and inclination angles of cracks were successfully reproduced in FE calculations. The position of a critical inclined localized zone where the bond failure began (close to the mid-shear span) was in agreement with the experimental observations in the beams SL20 and SL80. However, in the beams SL40, a small discrepancy was observed - the bond failure was closer to the support in FE simulations than in laboratory tests (Fig.13b).

Statistical simulations

For each beam size 12 statistical FE simulations with a random spatially correlated distribution of the local tensile strength f_t were performed. The assumed mean tensile strength and the standard deviation were kept constant independently of the beam size. The obtained mean nominal shear strengths v_c were as follows: 1.30 MPa, 1.01 MPa and 0.78 MPa in the beams SL20, SL40, and SL80. The statistical mean strengths were always lower than the corresponding deterministic values by approximately 10% regardless of the beam size (Fig.14). The reduction of the mean statistical shear strength (due to the material randomness) was independent of the beam size

and indicated that the statistical size effect did not take place.

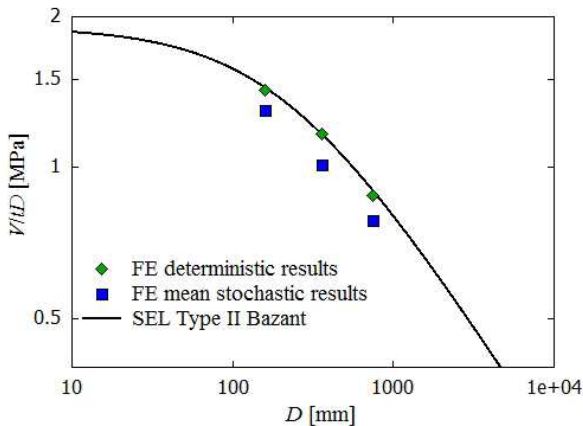


Figure 14: Nominal shear strengths of slender RC beams from FE deterministic and statistical simulations compared to SEL by Bazant

The calculated strain localization process followed in a similar way as in deterministic simulations. The fluctuation of a local tensile strength caused a non-symmetric distribution of localized zones and different paths of the bond failure (Fig.15).

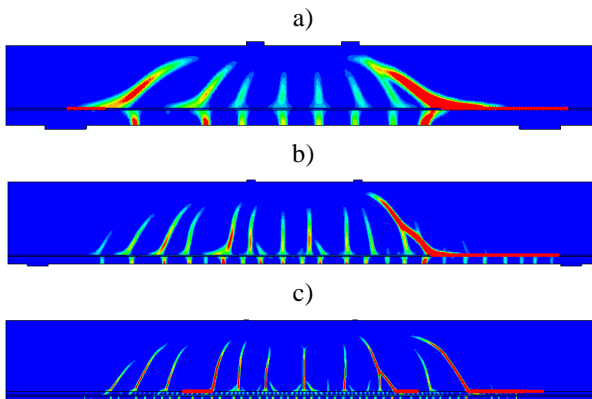


Figure 15: Calculated localized zones in statistical simulations: simulations in beam: SL20 (a), SL40 (b) and SL80 (c) (note that beams are not properly scaled)

4 CONCLUSIONS

The following conclusions can be drawn from our experimental and numerical investigations on the size effect of the shear strength in longitudinally reinforced slender and short concrete beams without shear reinforcement:

A pronounced size effect occurred in both slender and short reinforced concrete beams. The reduction of the nominal shear strength with increasing specimen height was stronger in short beams with basalt BFRP bars than in slender beams with steel reinforcement. The short beams with basalt bars were very brittle and the influence of the size on the strength was close to the solution given by LEFM. The crack width and beam deflection were higher in beams with BFRP than in beams with steel bars due to a lower modulus of elasticity. The experimental results agreed with the analytical size effect formula by Bazant. The width of localized zones on the concrete surface of slender RC beams measured with the DIC technique varied between $(1-1.5) \times d_{max}$ and was independent of the beam size.

An isotropic elasto-plastic constitutive model of concrete with non-local softening and characteristic length of microstructure could realistically reproduce the nominal shear strength reduction of RC beams with increasing beam height. The diagonal tensile failure mechanism of RC beams including the bond failure of a splitting type was captured with the bond-slip model by Akermann [26].

The mean shear strengths in statistical simulations were always lower than deterministic values by approximately 10% independently of the beam size. The size effect on the nominal shear strength was thus of a deterministic-energetic type only.

REFERENCES

- [1] Bazant Z., 1984. Size effect in blunt fracture: concrete, rock, metal. *J. Engng. Mech. ASCE*, **110**:518-35
- [2] Carpinteri A., 1989. Decrease of apparent tensile and bending strength with specimen size: two different explanations eased on fracture mechanics. *Int. J. Solids Structures* **25**(4):407-429
- [3] Bazant Z and Planas J., 1989. *Fracture and size effect in concrete and other quasi-brittle materials*. CRC Press LLC.

- [4] Leonhardt, F. and Walther, R., 1962. Schubversuche an Einfeldrigen Stahlbeton-Balken mit und ohne Schubbewehrung zur Ermittlung der Schubtragfähigkeit und der Oberen Schubspannungsgrenze. *Deutscher Ausschuss für Stahlbeton*, Heft 151, W. Ernst, u. Sohn, Berlin, 66
- [5] Kani, G.N.J., 1966. The basic facts concerning shear failure, *Proc. ACI J.*, **63**(7): 675–692
- [6] Kani, G.N.J., 1967. How Safe Are Our Large Concrete Beams? *ACI Journal, Proceedings*. **64**(3), 128-142
- [7] Bhal, N. S., 1968. *Über den Einfluss der Balkenhöhe auf Schubtragfähigkeit von einfeldrigen Stalbet.* Technische Hochschule, Otto-Graf-Inst.
- [8] Taylor, H.P.J., 1972. Shear Strength of Large Beams. *Journal of the Structural Division, ASCE*, **98**(ST11): 2473-2489
- [9] Walraven, J.C., 1978. The Influence of Depth on the Shear Strength of Lightweight Concrete Beams without Shear Reinforcement. *Stevin Laboratory Report No. 5-78-4*, Delft University of Technology
- [10] Chana, P.S., 1981. Some aspects of modelling the behavior of reinforced concrete under shear loading. *Tech. Rep. No.453*, Cement and Concrete Assoc., Wexham Springs
- [11] Iguro, M., Shioya, T., Nojiri, Y., and Akiyama, H., 1985. Experimental studies on shear strength of large reinforced concrete beams under uniformly distributed load. *Concrete Library Int. of JSCE*, **5**:137–146
- [12] Bazant, Z. and Kazemi, M.T., 1991. Size Effect on Diagonal Shear Failure of Beams without Stirrups. *ACI Structural Journal* **88**(3):268-276
- [13] Shioya, T., and Akiyama, H., 1994. Application to design of size effect in reinforced concrete structures. In Mihashi et al. (eds), *Size effect in concrete structures*. Spon, London, 409–416
- [14] Kim, J.K. and Park, Y.D., 1994. Shear strength of reinforced high-strength concrete beams without web reinforcement. *Magazine of Concrete Research*, **46**
- [15] Grimm, R., 1997. Einfluß bruchmechanischer kenngrößen auf das biege- und schubtragverhalten hochfester betone. Diss., Fachb. Konstr. Ingenieurbau der TH Darmstadt, 1996 und DafStb H.477, Beuth Verlag GmbH, Berlin
- [16] Ghannoum, W.M. 1998. Size effect on shear strength of reinforced concrete beams. *M.A.Sc Thesis*, MC Gill University, Department of Civil Engineering and Applied Mechanics, Montreal, Canada
- [17] Kawano, H. and Watanabe, H., 1997. Shear strength of reinforced concrete columns -Effect of specimen size and load reversal. In *Proc. 2nd Italy-Japan Workshop on Seismic Design and Retrofit of Bridges*, Rome, Italy, 27-28 February 1997: 141-154.
- [18] Podgorniak-Stanik, B.A., 1998. The influence of concrete strength, distribution of longitudinal reinforcement, amount of transverse reinforcement and member size on shear strength of reinforced concrete members. *M.A.Sc. Thesis*, Dept. of Civil Engineering, Univ. of Toronto
- [19] Yoshida, Y., 2000. Shear reinforcement for large lightly reinforced concrete members. *MASc Thesis*. Toronto, Canada: Department of Civil Engineering, University of Toronto.
- [20] Lubell, A., Sherwood, T., Bentz, E. and Collins, M., 2004. Safe shear design of

- large, wide beams. *Concrete International*, **26**(1): 66-78
- [21] Kozicki, J. and Teichman, J. (2007). Experimental investigations of strain localization in concrete using Digital Image Correlation (DIC) technique. *Archives of Hydro- Engineering and Environmental Mechanics* **54**:1, 3-24.
- [22] Syroka-Korol, E., Teichman, J. and Mróz, Z. FE calculations of a deterministic and statistical size effect in concrete under bending within stochastic elasto-plasticity and non-local softening. *Engineering Structures*, 2012 (in print).
- [23] Korol E., 2012. Theoretical and experimental study on size effect in concrete beams reinforced with steel or basalt bars. *PhD Thesis*. Gdansk University of Technology.
- [24] Teichman, J. and Bobiński, J., 2012. *Continuous and discontinuous modelling of fracture in concrete using FEM*. Springer, Berlin-Heidelberg.
- [25] Hordijk, D.A., 1991. Local approach to fatigue of concrete, *PhD dissertation*, Delft University of Technology
- [26] Brinkgreve, R. B. J., 1994. Geomaterial models and numerical analysis of softening. *PhD Thesis*, Delft University of Technology
- [27] Akkermann, J., 2000. Rotationsverhalten von Stahlbeton-Rahmendecken. *Dissertation*, University of Karlsruhe, Germany
- [28] Den Uijl, J. A. and Bigaj, A., 1996. A bond model for ribbed bars based on concrete confinement. *Heron* **41**(3):201–226.
- [29] Bobinski, J. and Teichman, J., 2004. Numerical simulations of localization of deformation in quasi-brittle materials within non-local softening plasticity. *Computers and Concrete* **4**:433-455
- [30] Karhunen, K., 1947. Über lineare Methoden in der Wahrscheinlichkeitsrechnung. *Ann. Acad. Sci. Fennicae. Ser. A. I. Math.-Phys.* **37**:1–79
- [31] Loève, M., 1948. Functions aleatoires du second ordre. Supplement to P.Levy, *Processus Stochastic et Mouvement Brownien*, Paris, Gauthier Villares
- [32] Phoon, K.K., Huang, S.P. and Quek, S.T. 2002a. Simulation of second-order processes using Karhunen–Loeve expansion. *Computers and Structures* **80**:1049–1060
- [33] Phoon, K.K., Huang, S.P. and Quek, S.T. 2002b. Implementation of Karhunen–Loeve expansion for simulation using a wavelet-Galerkin scheme. *Probabilistic Engineering Mechanics* **17**:293–303